Pergamon

Acta mater. Vol. 46, No. 16, pp. 5973–5984, 1998

Printed in Great Britain
PII: S1359-6454(98)00218-3
1359-6454/98 $19.00 + 0.00

MICROSTRUCTURE AND MECHANICAL PROPERTIES OF A CAST AND WIRE-DRAWN TERNARY Cu–Ag–Nb *IN SITU* COMPOSITE

D. RAABE[1]† and D. MATTISSEN[2]

[1]Department of Materials Science and Engineering, Wean Hall, Carnegie Mellon University, Pittsburgh, PA 15213-3890, U.S.A. and [2]Institut für Metallkunde und Metallphysik, Kopernikusstr. 14, RWTH Aachen, 52056 Aachen, Germany

(Received 26 August 1997; accepted 25 February 1998)

Abstract—A ternary *in situ* metal matrix composite consisting of Cu, 8.2 wt% Ag and 4 wt% Nb was produced by inductive melting, casting, and subsequent wire drawing. The material was very ductile so that a maximum wire strain of $\eta = 10.5$ was attained without intermediate annealing ($\eta = \ln(A_0/A)$, where A is the wire cross-section). The wire has a very high strength (1840 MPa at $\eta = 10.5$) and at the same time good electrical conductivity (46% of the conductivity of pure Cu). The wire strength is much larger than predicted by the linear rule of mixtures. Up to wire strains of $\eta \approx 8$ the strength even exceeds that of Cu–20 wt% Nb. The paper concentrates on the investigation of the evolution of the filament microstructure during wire drawing and its relation to the observed mechanical properties. The strength is discussed in terms of a Hall–Petch- or phase-barrier-type effect that arises from lattice dislocation pile-ups at the interfaces. © *1998 Acta Metallurgica Inc. Published by Elsevier Science Ltd. All rights reserved.*

1. INTRODUCTION AND MOTIVATION

Binary metal matrix composites (MMC) consisting of Cu as matrix and a high melting body centered cubic (b.c.c.) transition metal (e.g. Nb, Mo, Ta, V, W, Cr) [1–12] or face centered cubic (f.c.c.) Ag [13–19] as second phase have attracted much attention. This is mainly due to two reasons. First, they are promising material candidates in robotics [20] and high field magnet design [21–27], since after heavy deformation very high strength combined with good electrical conductivity can be achieved. Second, they serve as model composites for the investigation of fundamental mechanisms that determine the observed relations between microstructure and mechanical and electrical properties. For instance, in the field of mechanics, the Hall– Petch-type interaction of lattice dislocations with interfaces [28, 29] and the generation of geometrically necessary dislocations [6, 8, 30, 31] are considered as important mechanisms for the explanation of the enormous strength observed. In the field of electronics, the interaction mechanisms of conduction electrons and Cooper-pairs (in Nb) with the interfaces are assumed to mainly determine the resistive conductivity [1, 2] and the superconductivity of the bulk material [32–34].

In the last two decades particular emphasis was placed on the investigation of binary Cu–Nb [1–12] and Cu–Ag alloys [13–19]. In the first case (Cu–Nb) the two constituents have negligible mutual solubility and form a quasi-monotectic system [35, 36]. During casting the Nb solidifies with dendritic morphology. Upon wire drawing the dendrites form into fibers the spacing of which continuously drops with increasing strain. Alloys consisting of Cu and 20% Nb‡ reveal an ultimate tensile strength (UTS) of up to 2.2 GPa ($\eta = 12$) [4, 5, 9, 10]. An increased Nb content leads to a decrease in ductility and to a degradation of the electrical conductivity. In the second case (Cu–Ag) the two constituents reveal a single immiscibility gap, leading to the formation of a simple eutectic equilibrium phase diagram with limited mutual solubility [37]. Previous investigations on a Cu alloy containing more than 6% Ag have shown that this MMC consists of two phases, a Cu-rich solid solution and a Cu–Ag eutectic. During deformation the eutectic and the Cu-rich matrix form into lamellar filaments where the interlamellar spacing decreases with wire strain. An intermediate heat treatment leads to Ag precipitations. These can be used to increase the matrix strain and/or to form additional fibers during further drawing. After large wire strains Cu–Ag MMCs reveal an UTS of up to $\sigma = 1.5$ GPa ($\eta = 10$) [14, 15]. As in the case of Cu–Nb, the enormous increase in strength of Cu–Ag exceeds that predicted by the linear rule of mixtures. The profile of strength and conductivity of near-eutectic

†To whom all correspondence should be addressed. Present address: Luchweg 10, 14621 Schönwalde, Germany.

‡If not stated otherwise "%" means "wt%"

Cu–Ag alloys shows a similar dependence on wire strain as the Cu–Nb alloys. When the interface spacing in the heavily deformed *in situ* MMCs is reduced to the order of the mean free electron path, the conductivity of both alloy types drops with further deformation. Due to the high intrinsic conductivity of the constituents and the comparatively small contribution of inelastic interface scattering, eutectic Cu–Ag MMCs reveal, at a given strength level, a somewhat better conductivity than Cu–Nb alloys.

As a logical consequence of these efforts on binary MMCs, and in continuation of the pioneering experiments of Spitzig [38], this paper introduces a new generation of ternary Cu–Ag–Nb composites with the aim to combine the hardening effects of both phases, and at the same time simplify the processing and drop the production costs. The alloy was processed by an induction melting technique and manufactured by wire drawing at room temperature without annealing. Due to the low Nb content the melting point is much below that of the classical Cu–20%Nb composite.

For a given chemical composition the filament morphology and topology chiefly determine the strength and the electrical properties of MMCs. This paper thus concentrates on the investigation of the microstructural evolution during processing. The obtained data are used to explain the observed mechanical properties. The relation of microstructure and electrical properties will be discussed in an ensuing paper [39].

2. EXPERIMENTAL PROCEDURE

2.1. Material processing

The Cu–8.2% Ag–4% Nb alloy was melted in an induction furnace at a frequency of 10 kHz and a power of 50 kW [40]. All ingredients had an initial purity of at least 99.99%. Ingots of 18 mm diameter were cast under an argon atmosphere at a pressure of 0.6×10^5 Pa. Since no experimental ternary phase diagram of Cu–Ag–Nb has been published, the binary phase diagrams of Cu–Nb and Cu–Ag had to be taken into account. According to the Cu–Nb system [35, 36] a melting temperature of at least 1500°C is recommended for a Cu alloy with 4% Nb. However, owing to the possibility of a miscibility gap in the liquid phase due to the presence of foreign interstitials [36], a peak temperature of 1830–1850°C was employed in order to assure complete dissolution of the Nb. For the cast, a crucible of high-purity graphite and a preheated Cu mould were used. From the cylindrical ingots wires were produced by rotary swaging and subsequent drawing through hard-metal drawing-bench dies without intermediate annealing. The final diameter was 0.1 mm corresponding to a true strain of $\eta = 10.5$. Further processing details are reported elsewhere [40].

2.2. Microscopy, specimen preparation, and mechanical testing

Optical and scanning electron microscopy (SEM) were employed to quantitatively investigate the morphology and topology of the Ag and Nb filaments. However, due to the insufficient contrast after etching, an unambiguous optical identification of the three phases was sometimes not possible. Thus, the specimens were additionally analyzed using energy-disperse X-ray spectrometry (EDX) in the SEM. For this investigation the samples were ground and subsequently etched using a solution of 50 ml C_2H_5OH, 50 ml HF, and 30 ml HNO_3. This etching removed the smeared-out Nb debris which had formed during grinding on the sample surface. Finally, the specimens were carefully polished. Each micrograph was then complemented with an EDX line scan for the identification of the Ag and Nb filaments. The morphology of the isolated Nb fibers was additionally investigated by use of a selective etching technique, where the Cu and Ag were dissolved by dilute nitric acid. The filament spacing was determined by an edge-to-edge measurement.

Verhoeven *et al.* [41, 42] have shown that the MMC filament data determined by use of SEM are at large strains less accurate than those obtained by use of transmission electron microscopy (TEM). It must thus be considered that the true filament diameters might at large strains be smaller than those observed in the SEM.

Vickers hardness measurements were carried out on samples which were prepared in the same way as described above. Tensile tests on deformed wire samples were conducted at 298 K and at 77 K. Weakly deformed specimens ($\eta \leq 5.5$) were tested using a 100 kN tensile machine. Heavily deformed specimens ($\eta > 7.5$) were tested using a smaller tensile machine which was equipped with a load cell and a linear variable displacement transducer. At least three tensile experiments were carried out on each wire.

3. EXPERIMENTAL RESULTS

3.1. Microstructure

3.1.1. As-cast state. Figure 1 shows the microstructure of the as-cast Cu–8.2% Ag–4% Nb alloy. The Ag had a lamellar shape and formed a Ag–Cu eutectic. Some of these eutectic domains solidified around the primary Nb. In Fig. 2, where the matrix and the Ag were removed by selective etching, one can see isolated Nb Wulff polyhedra [Fig. 2(a)] and dendrites [Fig. 2(b)]. The average diameter of the Nb particles in the as-cast state amounted to $d_{Nb} \approx 1481$ nm.

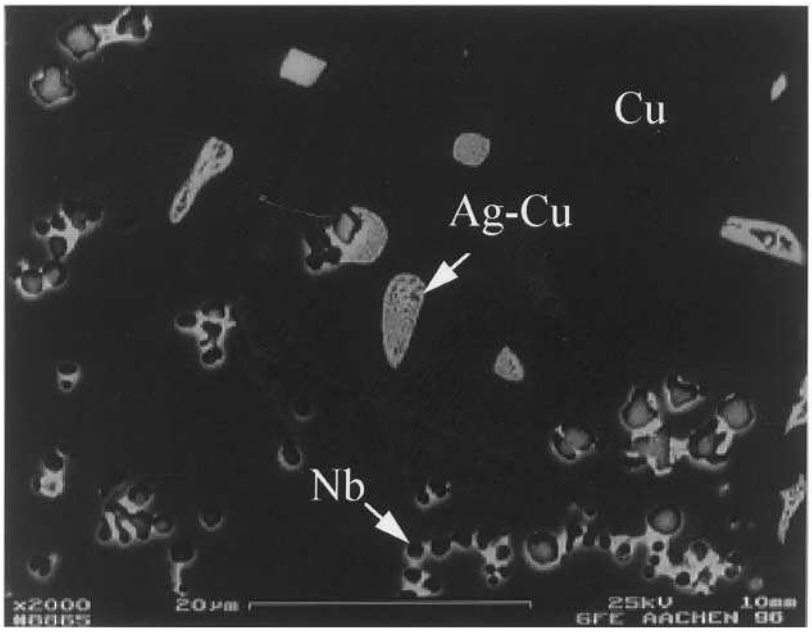

Fig. 1. SEM micrograph of as-cast Cu–8.2% Ag–4% Nb, cross-section, Nb and Ag–Cu eutectic embedded in Cu matrix (% = wt%).

3.1.2. Evolution of the Nb phase during wire drawing. Figure 3 shows the morphological evolution of the Nb polyhedra and dendrites into filaments. At low strains ($\eta \leq 4$), the Nb morphology appeared inhomogeneous [Fig. 3(a)]. While some dendrite arms revealed considerable elongation, others appeared almost undeformed. With increasing deformation ($4 < \eta < 10.5$), the filament morphology became more uniform [Fig. 3(b)–(d)]. At the maximum strain ($\eta = 10.5$) the fibers had an average diameter of $d_{Nb} \approx 66$ nm [Fig. 3(d)]. The smallest observed filaments had a thickness below 33 nm. The random distribution of the dendrites [Fig. 3(a)–(d)] is an artifact which stems from sample preparation. Figure 4 shows the Nb filament diameter, d_{Nb}, as a function of the wire strain. Using an exponential fit, these data can be approximated by $d_{Nb} = 1386.6 \text{ nm} \times \exp(-0.4143\,\eta)$.

3.1.3. Evolution of the Ag phase during wire drawing. Figure 5 shows a backscatter micrograph of the wire together with an EDX line scan for the identification of Ag and Nb ($\eta = 3.6$). The filaments are aligned parallel to the wire axis. At such low strains the Ag filaments were shorter and thicker than the Nb filaments. With increasing deformation their morphology became more similar to that of the Nb. At a wire strain of $\eta = 3.6$ the average Ag filament diameter amounted to $d_{Ag} \approx 676$ nm and at $\eta = 6$ to $d_{Ag} \approx 260$ nm (Fig. 4). Using an exponential fit, these data can be approximated by $d_{Ag} = 2630 \text{ nm} \times \exp(-0.3861\,\eta)$.

3.1.4. Evolution of the filament spacing and deformation homogeneity. The spacing between the filaments drops with increasing degree of wire deformation (Fig. 6). Using an exponential fit, the average fiber spacing can be described by $d_{Cu} = 31\,767 \text{ nm} \times \exp(-0.6415\,\eta)$.

Figure 7 shows the thickness reduction of the Nb filaments, as measured from the metallographic data, as a function of the wire deformation. At low and intermediate strains the Nb carries less deformation than expected for homogeneous wire deformation. For instance, a wire strain of $\eta \approx 6$ corresponds to an actual Nb filament strain of only $\eta \approx 5$. With increasing strain the curve seems to proceed towards a saturation of the Nb filament thickness. However, the Nb data at large strains might be below those observed, due to the limited SEM resolution. If not explicitly stated otherwise, hereafter, η will be used to indicate the wire deformation.

3.2. Mechanical properties

Figure 8 shows the Vickers hardness (200 g) as a function of strain. The as-cast material had a hardness of about HV 101.5. At the largest attained strain ($\eta = 10.5$) the hardness amounted to HV 396.9. The hardness reaches a weak plateau of HV 330 at $7 \leq \eta \leq 9$. After that the hardness increases again. The data scatter at $\eta = 10.5$ is due to the reduced wire dimension, which made the measurements less accurate. At all strains the indentation cup showed a systematic distortion. The radial impression diameter was always larger than in the wire axis direction, i.e. the hardness in radial direction was below that parallel to the wire axis.

Figure 9 shows the stress–strain curves of wires that were drawn to strains between $\eta = 8$ and 10.5 at 298 K. The slope before the yield strength suggests an elastic modulus of about 106.2 GPa.

Figure 10 presents the effect of wire deformation on the UTS for samples tested at 298 K and 77 K. At 298 K the UTS reaches a value of 925.7 ± 5 MPa for a wire that was drawn to $\eta = 4$. With increasing wire deformation prior to the tensile test the UTS exponentially increases and reaches a maximum value of 1841 ± 7 MPa at $\eta = 10.5$. The data show a plateau at $8.5 \leq \eta \leq 9$. The UTS is 320 MPa larger at 77 K than at 298 K (Fig. 10).

The mechanical results obtained from the Vickers hardness measurements do not linearly correspond to those obtained from the tensile tests. The reason for this discrepancy is that the radial Vickers indentation yields an anisotropic plastic response and that the stress state is less well defined than in a tensile test. In the discussion we will thus mainly make use of the data obtained from the tensile tests.

4. DISCUSSION

4.1. Microstructure in the as-cast state

The fact that the Nb solidified with a dendritic and a polyhedral morphology can be attributed to the large overheating of the melt, the enormous

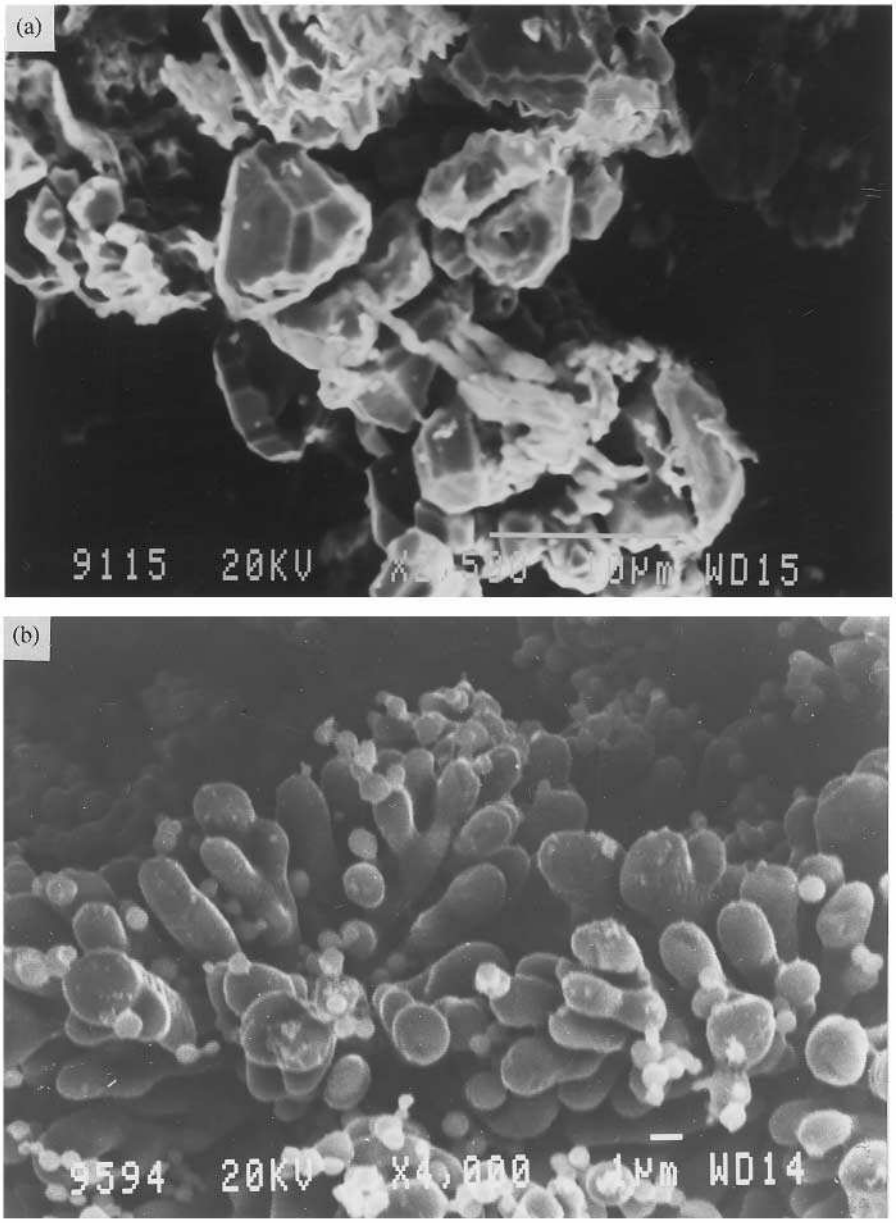

Fig. 2. SEM micrographs of as-cast Cu–8.2% Ag–4% Nb, Cu and Ag dissolved by selective etching. (a) Nb Wulff polyhedra; (b) Nb dendrites (% = wt%).

temperature difference that exists in the solidification of the Nb and the Cu and Ag, and the low Nb content. The diameter of the Nb particles in the as-cast state ($d_{Nb} \approx 1481$ nm) is relatively small when compared to binary Cu–Nb composites [1–12]. The existence of a Ag–Cu eutectic indicates that the maximum solubility of Ag in Cu was exceeded. The published maximum equilibrium solubilities of Ag in Cu vary between 7% (4.25 at.%) and 10% (6.14 at.%) at 779°C [13–19, 37]. Due to the high quenching rate and the absence of any precipitation heat treatment after casting, it is likely that some Ag was still solute in the Cu matrix. This could be exploited in conducting further optimization of the composite [18].

4.2. Morphological evolution of the Nb and Ag phase during wire drawing

The inhomogeneous Nb morphology observed at low strains ($\eta \leq 4$) [Fig. 3(a)] shows that heavy deformation is necessary to produce a homogeneous size distribution of the Nb filaments. This can be attributed to several reasons. First, the strain distribution during wire drawing is inhomogeneous

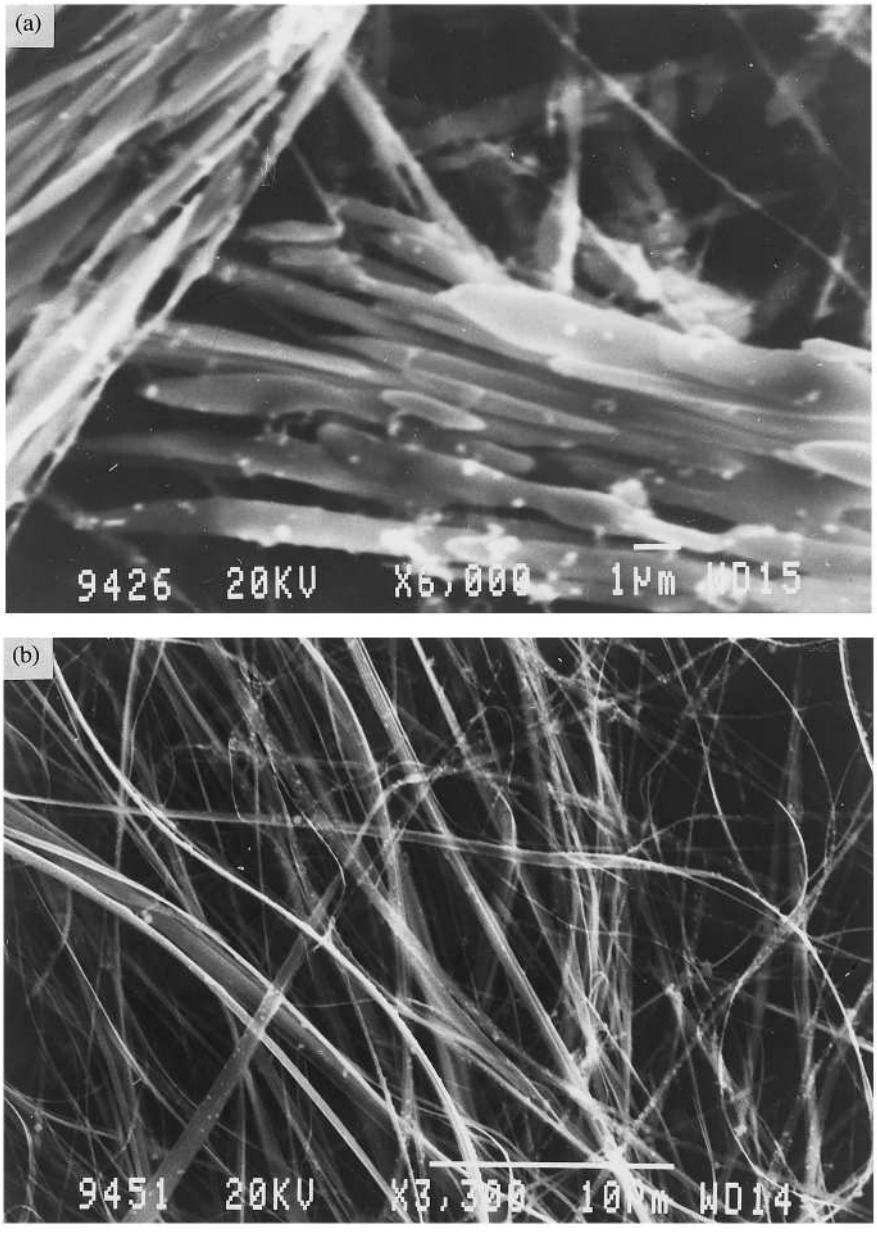

Fig. 3(a)–(b) *(caption overleaf)*

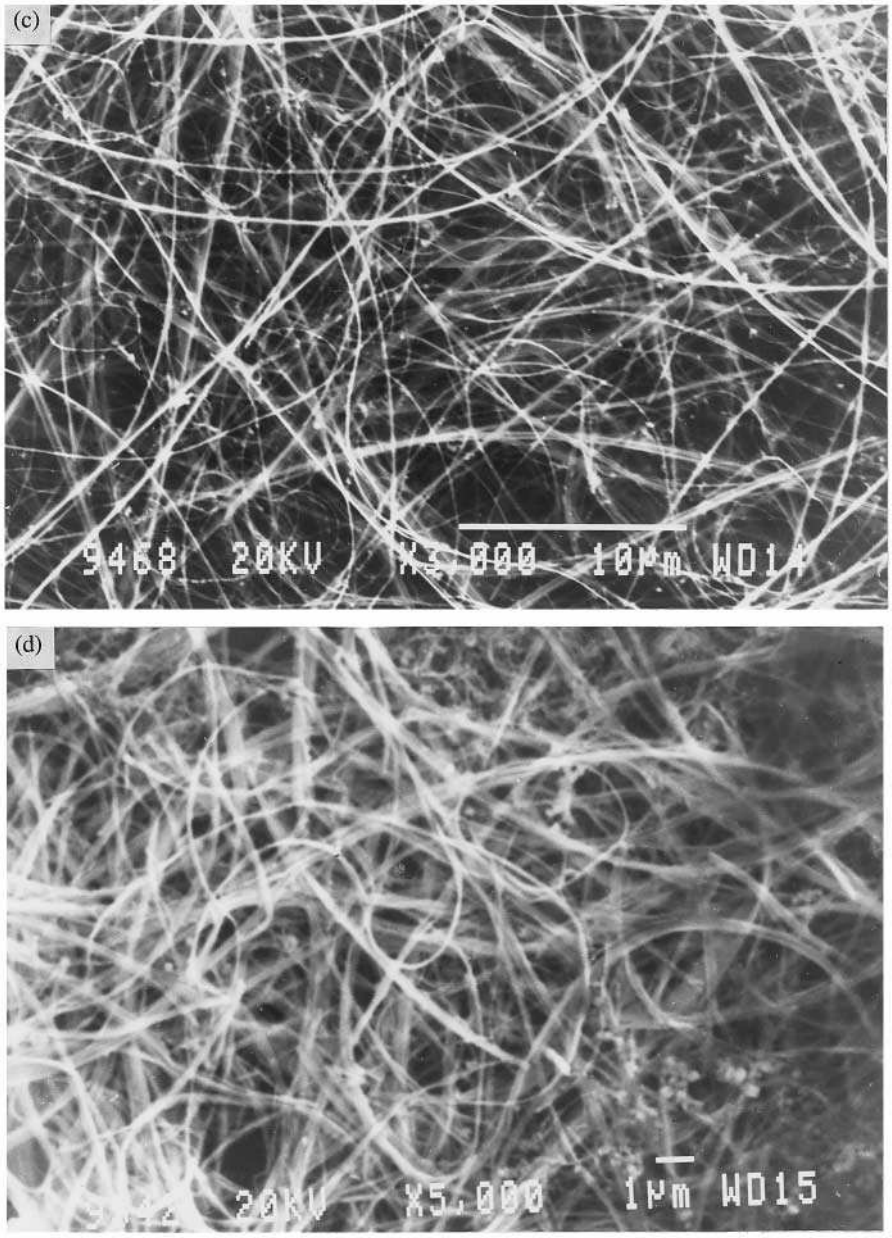

Fig. 3. SEM micrographs of Nb filaments, Cu and Ag dissolved by selective etching. (a) $\eta = 2.6$; (b) $\eta = 4$; (c) $\eta = 6$; (d) $\eta = 10.5$.

across the wire diameter due to surface friction. Second, the equiaxed Nb polyhedra [Fig. 2(a)] undergo at low and intermediate strains a different shape change than the elongated Nb dendrites [Fig. 2(b)]. At small wire strains the polyhedra deform into elongated filaments, whereas the randomly oriented dendrites at first align parallel to the wire axis. After this alignment a massive cross-sectional area reduction of the dendrites takes place [e.g. Fig. 3(c)]. Furthermore, the deformation is strongly influenced by the plastic incompatibility of the three interacting phases. Since the Nb has an inhomogeneous spatial distribution and undergoes an average deformation below that of the wire (Fig. 7), the more ductile f.c.c. phases must undergo a higher deformation, locally. This again modifies the local stress distribution within the wire, i.e. neither the actual Cu strain nor the actual Ag or Nb strain equals the true wire strain.

The Ag–Cu eutectic formed into elongated filaments from the beginning of wire deformation. Since the average Ag filament diameter was always larger than that of the Nb [Fig. 4(a)], one can assume that the specific Hall–Petch contribution of the Ag to the overall strength is below that of the Nb. In the present alloy this lack was compensated

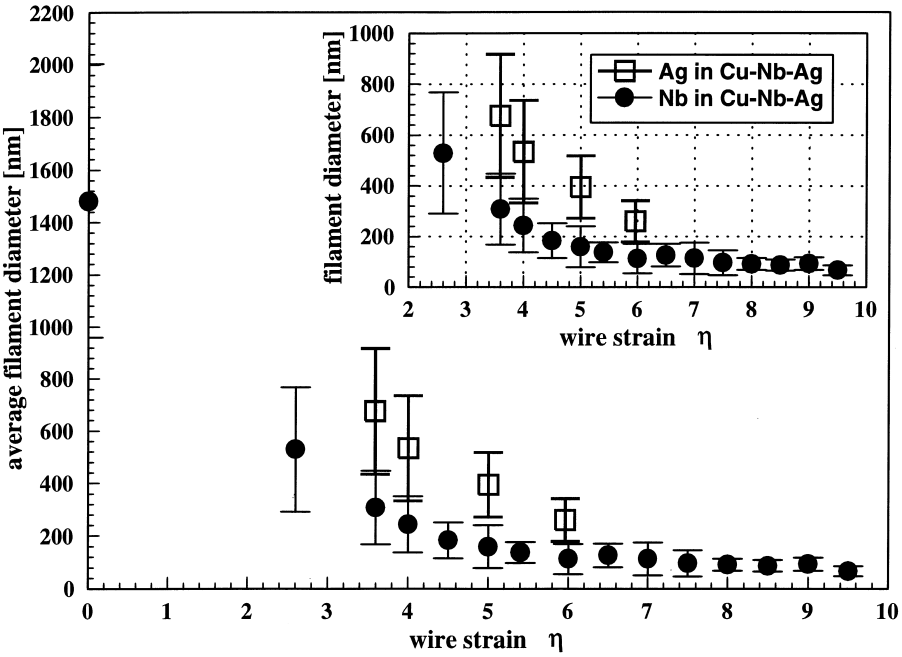

Fig. 4. Average filament diameter of Nb and Ag in Cu–8.2% Ag–4% Nb as a function wire strain (% = wt%).

for by an increased Ag content. Raising the Ag (8.2%) instead of the Nb (4%) content is reasonable for two reasons. First, Ag decreases the melting point of Cu, while Nb drastically increases it. This is important with respect to the production of such materials. Second, the Cu–Ag interfaces have a smaller contribution to inelastic scattering of conduction electrons than the Cu–Nb interfaces. This is an essential criterion since *in situ* MMCs are developed because of their combination of high strength and good conductivity. The ternary MMC wires reach a room temperature UTS of 1846 MPa (Figs 9 and 10) and at the same time 46% of the conductivity of pure Cu (46% IACS where IACS is the International Annealed Cu Standard). Although the total alloy content amounts to only 12.2%, this property profile exceeds that of the classical Cu–20% Nb MMC.

4.3. Geometrically necessary dislocations

At strains above $\eta \approx 4$ the Nb and Ag filaments are aligned parallel to the wire axis. The strong Nb filament bending that can be observed after removing the strain constraints through dissolving the Cu

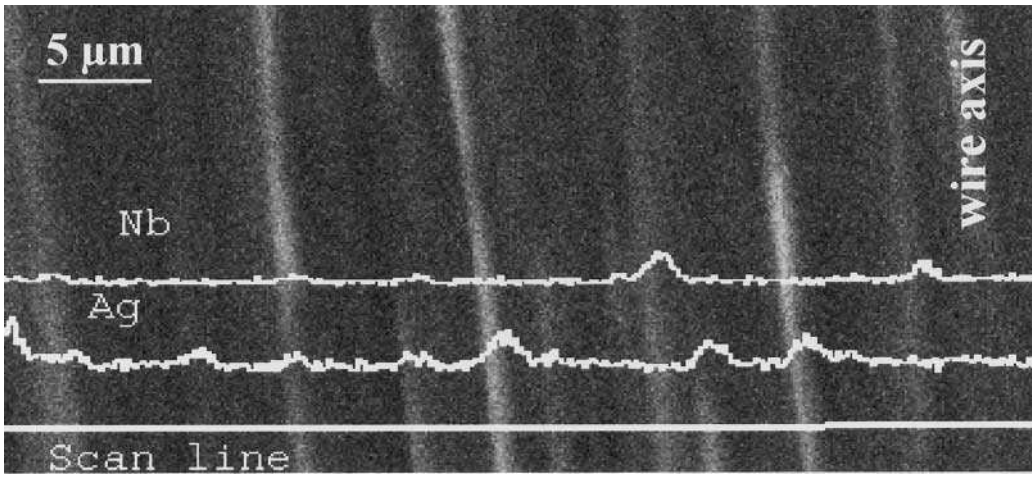

Fig. 5. SEM micrograph with EDX line scan of Cu–8.2% Ag–4% Nb (% = wt%).

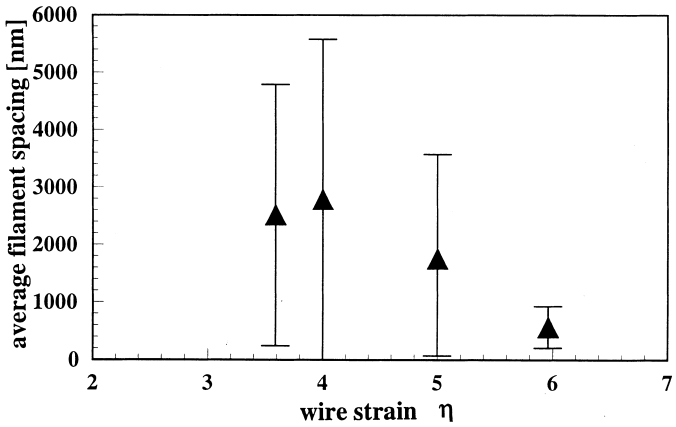

Fig. 6. Average filament spacing in Cu–8.2% Ag–4% Nb as a function wire strain (% = wt%).

and Ag indicates residual stresses, i.e. a certain content of geometrically necessary dislocations (GNDs) within the Nb [e.g. Fig. 3(c) and (d)]. Each dislocation is a localized source of long-range displacement fields. The skew-symmetric part of the net displacement gradient tensor that may result from superimposing the displacement fields of many such lattice defects directly corresponds to the lattice curvature. We refer to those dislocations that contribute to the observed long-range bending as first-order or lattice GNDs. It is likely that similar dislocation arrangements are also present in the Ag.

Although their overall density is presumably relatively low compared to that of the statistically stored dislocations, Funkenbusch and Courtney interpreted the strength of binary MMCs in terms of such GNDs [6, 8]. The basic origin of GNDs was in their work attributed to the incompatibility between the body centered and the face cubic phase [6, 8]. It can also be understood in the framework of a physical Hall–Petch-type model [28, 29]. This phase-barrier approach, which is in the form of a modified linear rule of mixtures, accounts for dislocation pile-ups in the Cu matrix and for the activation of dislocation sources in the filaments under consideration of the texture and filament geometry [29]. It predicts that the pile-up mechanism can lead to certain arrays of GNDs in the filaments and in the matrix.

Due to the magnitude of the curvatures observed and the low overall content of Nb and Ag, however, we do not interpret the strength of our alloy in terms of these first-order GNDs, but in terms of the more plausible phase-barrier mechanism.

For explaining the strength of binary MMCs at very large wire strains, where ordinary dislocation

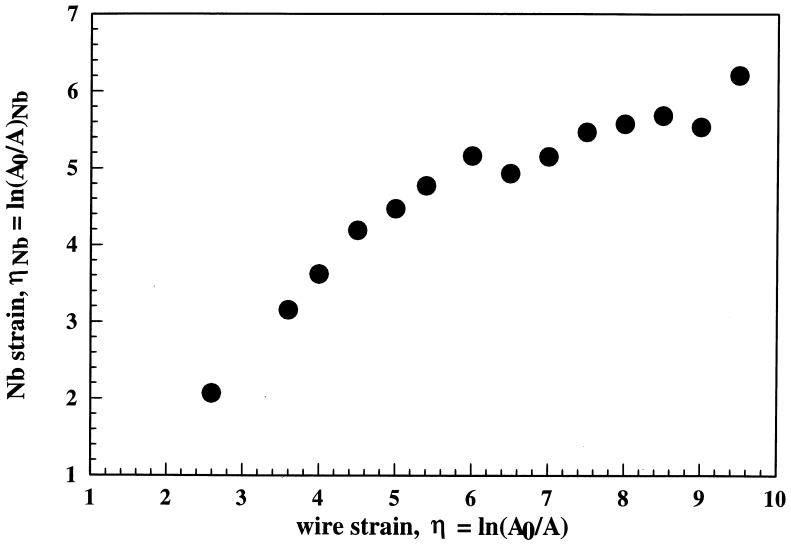

Fig. 7. Nb strain η_{Nb} as a function of wire strain η.

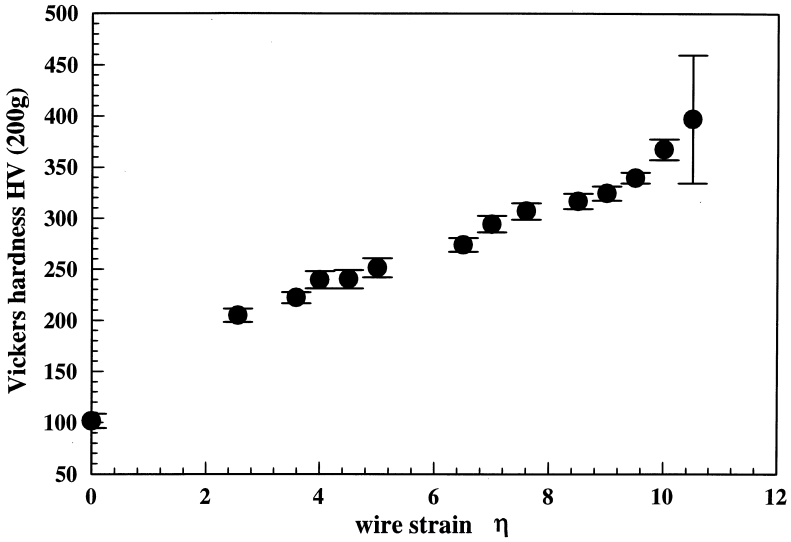

Fig. 8. Vickers microhardness (200 g) of Cu–8.2% Ag–4% Nb as a function of wire strain (% = weight%).

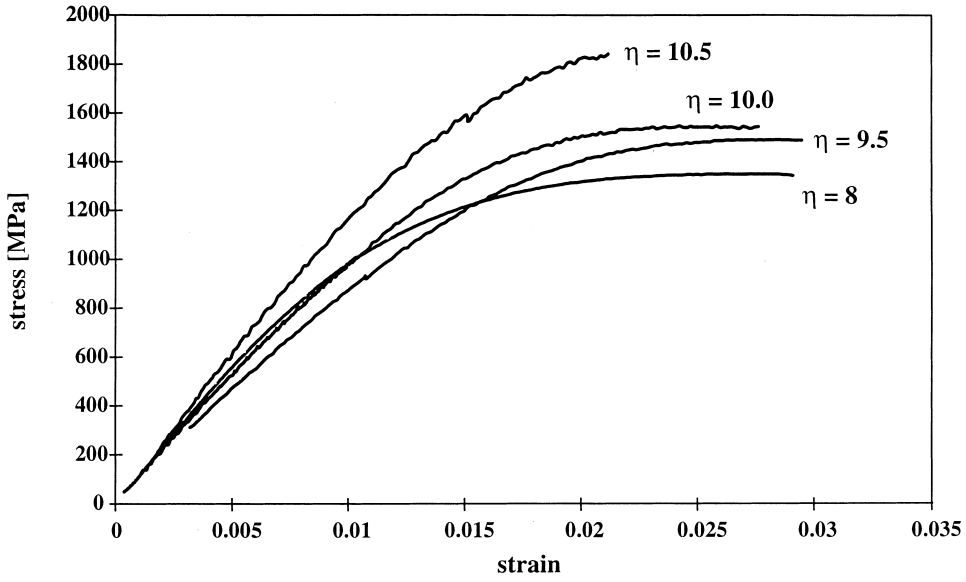

Fig. 9. Stress–strain curves of Cu–8.2% Ag–4% Nb wires at various wire deformations (% = wt%).

sources can no longer be activated in the fibers [28], but some ductility is still observed, a simple Hall–Petch model does apparently no longer work. Embury and coworkers [30, 31] thus proposed that moving matrix dislocations might penetrate the filaments under generation of geometrically necessary interface dislocations. We refer to them here as second-order GNDs.

Due to the limited spatial resolution of the present electron optical data, it cannot be clearly decided to which class of GNDs the observed bending can be assigned. It is likely though, since the bending already occurs at intermediate strains, where dislocation sources are still active in the filaments, that the observed shape changes (not the flow stress) might be mainly due to first-order GNDs.

4.4. Microstructure and mechanical properties—comparison between the ternary Cu–Ag–Nb MMC and the binary Cu–Nb MMC

Figure 11 shows that the average diameter of the Nb filaments in the investigated ternary Cu–Ag–Nb alloy is smaller than in many comparable binary Cu–20% Nb alloys.† This applies not only for the average diameter in the as-cast state but also for

†The Nb filament data for the Cu–20% Nb MMC were taken from the paper of Heringhaus *et al.* [12]

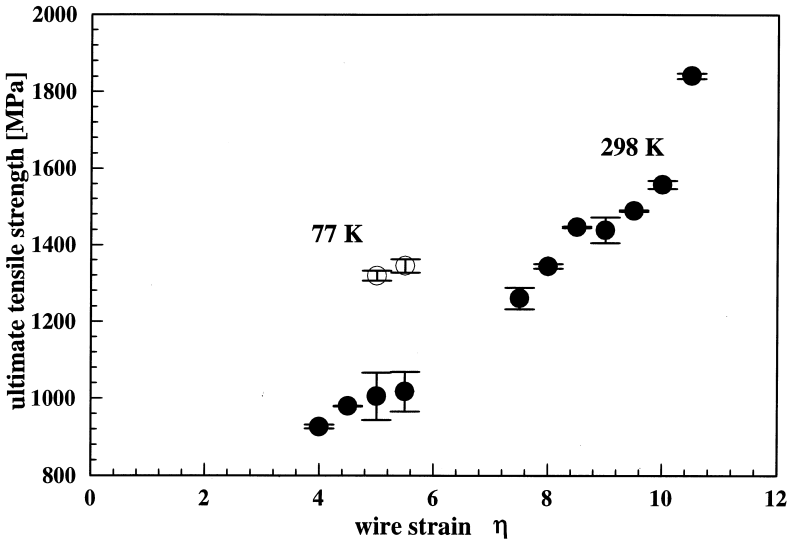

Fig. 10. Ultimate tensile strength of Cu–8.2% Ag–4% Nb wires at various wire deformations at 298 K and 77 K (% = wt%).

the further thickness decrease during wire drawing. A comparison of the fitted curves shows that the exponential drop of the Nb filament thickness is even steeper in the ternary than in the binary alloy. The ternary material thus contains small Nb filaments already at medium wire strains ($\eta \approx 4$–6) with a thickness below those observed in the binary MMC. This evolution has two advantages. First, the various physical [28, 29, 43] and empirical models [4, 5, 9, 44] predict a Hall–Petch-type increase in strength, inversely proportional to the square root of the interface spacing. Second, the rapid refinement in fiber scale as a function of wire strain (Fig. 11) provides advantageous properties already at medium wire strains. This aspect is particularly relevant, since in most electromagnetic applications exceedingly thin wire dimensions are to be avoided. The effect of these microstructural improvements with respect to earlier alloys is demonstrated in Fig. 12, which shows the UTS as a function of wire strain for Cu–8.2% Ag–4% Nb and two Cu–20% Nb alloys [42] with different Nb dendrite diameters in the as-cast state. This diagram substantiates that the UTS of the ternary material

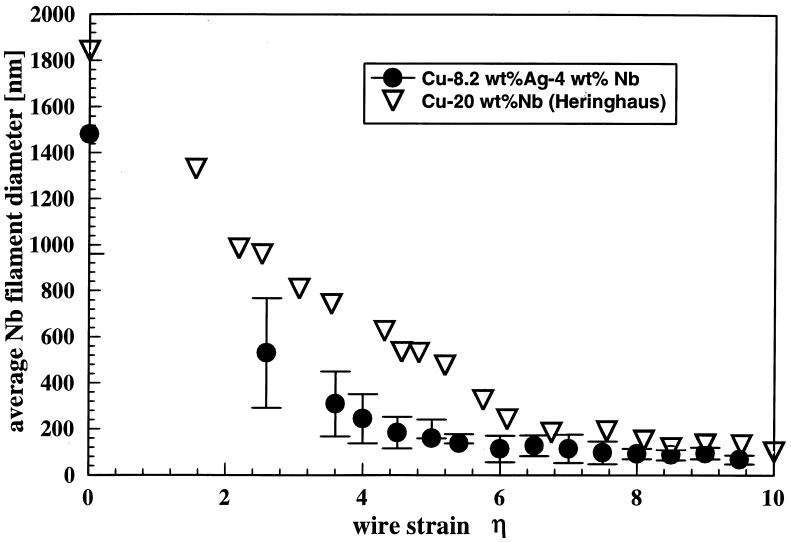

Fig. 11. Average filament diameter of Nb in Cu–8.2% Ag–4% Nb and in Cu–20% Nb as a function wire strain (Cu–20% Nb data from Ref. [12]; % = wt%).

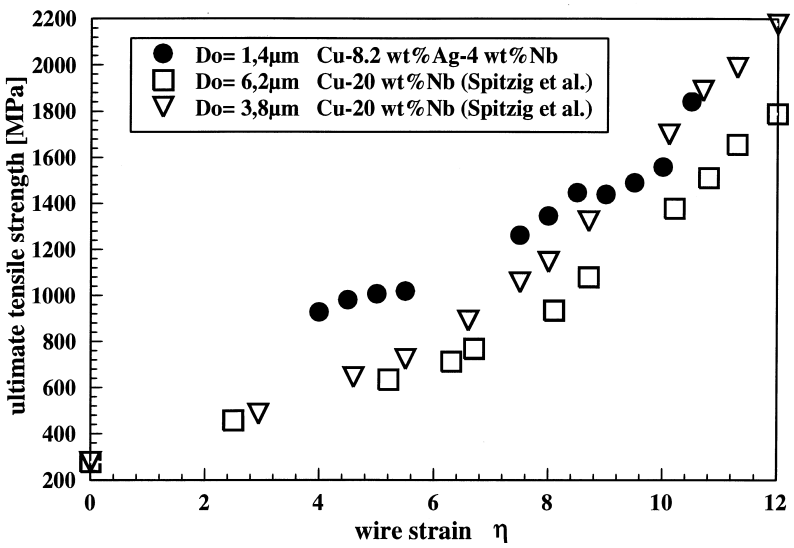

Fig. 12. Ultimate tensile strength of Cu–8.2% Ag–4% Nb and two Cu–20% Nb alloys with different Nb dendrite diameters in the as-cast state (Cu–20% Nb data from Ref. [42]; % = wt%).

with a total alloy content of only 12.2% exceeds that of Cu-20% Nb up to wire strains of $\eta \approx 8$. At larger strains it shows a similar strength as Cu–20% Nb with an initial dendrite diameter of 3.8 μm.

5. CONCLUSIONS

A ternary *in situ* Cu–8.2 wt% Ag–4 wt% Nb MMC was manufactured by melting, casting, and wire drawing. The microstructure was investigated using electron microscopy and EDX. The mechanical properties were determined using tensile and hardness tests. The main results are:

- The material was very ductile. A maximum wire strain of $\eta = 10.5$ was reached without annealing.
- Wires of maximum strain had an UTS of 1840 MPa and 46% of the conductivity of pure Cu (IACS).
- The wire strength was much larger than predicted by the linear rule of mixtures, up to $\eta \approx 8$ the UTS was even larger than that of Cu–20 wt% Nb.
- The observed mechanical properties were discussed in terms of a Hall–Petch- or phase-barrier-type effect that arises from lattice dislocation pile-ups at the interfaces.

Acknowledgements—The authors are indebted to F. Heringhaus, J. D. Embury, and G. Gottstein for helpful comments and stimulating discussions. The support by the National High Magnetic Field Laboratory, Tallahassee, Florida, where some of the experiments were carried out has to be mentioned with gratitude. One of the authors (D.R.) gratefully acknowledges the financial support by the Deutsche Forschungsgemeinschaft through the Heisenberg program and the kind support by the Department of Materials Science and Engineering at Carnegie Mellon University.

REFERENCES

1. Bevk, J., Harbison, J. P. and Bell, J. L., *J. appl. Phys.*, 1978, **49**, 6031.
2. Karasek, K. R. and Bevk, J., *J. appl. Phys.*, 1981, **52**, 1370.
3. Funkenbusch, P. D. and Courtney, T. H., *Acta metall.*, 1985, **33**, 913.
4. Spitzig, W. A., Pelton, A. R. and Laabs, F. C., *Acta metall.*, 1987, **35**, 2427.
5. Spitzig, W. A. and Krotz, P. D., *Scripta metall.*, 1987, **21**, 1143.
6. Funkenbusch, P. D., Lee, J. K. and Courtney, T. H., *Metall. Trans.*, 1987, **A18**, 1249.
7. Chumbley, L. S., Downing, H. L., Spitzig, W. A. and Verhoeven, J. D., *Mater. Sci. Engng*, 1989, **A117**, 59.
8. Funkenbusch, P. D. and Courtney, T. H., *Scripta metall.*, 1989, **23**, 1719.
9. Spitzig, W. A., *Acta metall.*, 1991, **39**, 1085.
10. Spitzig, W. A., Downing, H. L., Laabs, F. C., Gibson, E. D. and Verhoeven, J. D., *Metall. Trans.*, 1993, **A24**, 7.
11. Raabe, D., Heringhaus, F., Hangen, U. and Gottstein, G., *Z. Metallk.*, 1995, **86**, 405.
12. Heringhaus, F., Raabe, D. and Gottstein, G., *Acta metall.*, 1995, **43**, 1467.
13. Cline, H. E. and Lee, D., *Acta metall.*, 1970, **18**, 315.
14. Frommeyer, G. and Wassermann, G., *Physica status solidi (a)*, 1975, **27**, 99.
15. Frommeyer, G. and Wassermann, G., *Acta metall.*, 1975, **23**, 1353.
16. Sakai, Y., Inoue, K. and Maeda, H., *Acta metall.*, 1995, **43**, 1517.
17. Sakai, Y. and Schneider-Muntau, H.-J., *Acta metall.*, 1997, **45**, 1017.
18. Heringhaus, F., Ph.D. thesis, Institut für Metallkunde und Metallphysik, RWTH Aachen, Germany, and National High Magnetic Field Laboratory, Tallahassee, U.S.A., 1998.
19. Sohn, K. Y., Ph.D. thesis, Department of Materials Science and Engineering, University of Florida, Gainesville, U.S.A., 1997.

20. Raabe, D., Miyake, K. and Takahara, H., *Acta mater*., to be published.
21. Foner, S. and Bobrov, E., *I.E.E.E. Trans. Magn*., 1987, **24**, 1059.
22. Asano, T., Sakai, Y., Inoue, K., Oshikiri, M. and Maeda, H., *I.E.E.E. Trans. Magn*., 1992, **28**, 888.
23. Heringhaus, F., Eyssa, Y. M., Pernambuco-Wise, P., Bird, M. D., Gottstein, G. and Schneider-Muntau, H.-J., *Metall*., 1996, **50**, 272.
24. Embury, J. D., Hill, M. A., Spitzig, W. A. and Sakai, Y., *Mater. Res. Soc. Bull*., 1993, **8**, 57.
25. Heringhaus, F., Leffers, R., Gottstein, G. and Schneider-Muntau, H.-J., Processing, Properties, and Application of Cast Metal Matrix Composites, *TMS Fall Meeting*, Vol. 1, 1996, p. 127.
26. Schneider-Muntau, H.-J., *I.E.E.E. Trans. Magn*., 1982, **18**, 32.
27. Wood, J. T., Embury, J. D. and Ashby, M. F., *Acta mater*., 1997, **45**, 1099.
28. Sevillano, J. G., *J. Physique III*, 1990, **6**, 967.
29. Hangen, U. and Raabe, D., *Acta metall*., 1995, **43**, 4075.
30. Wood, J. T., Ph.D. thesis, McMaster University, Canada, 1994.
31. Embury, J. D., private communication, 1997.
32. Raabe, D. and Heringhaus, F., *Physica status solidi (a)*, 1994, **142**, 473.
33. Raabe, D. and Hangen, U., *Acta metall*., 1996, **44**, 953–961.
34. Raabe, D. and Hangen, U., *Physica status solidi (a)*, 1996, **154**, 715.
35. Chakrabati, D. J. and Laughlin, D. E., *Bull. Alloy Phase Diagrams*, 1982, **2**, 936.
36. Terekhov, G. I. and Aleksandrova, L. N., *Izv. Akad. Nauk SSSR*, 1984, **4**, 210.
37. Murray, J. L., *Metall. Trans*., 1984, **A15**, 261.
38. Spitzig, W. A., unpublished data.
39. Raabe, D., Mattissen, D. and Heringhaus, F., *Acta mater*., to be published.
40. Raabe, D. and Mattissen, D., *Metall*., 1997, **51**, 464.
41. Verhoeven, J. D., Spitzig, W. A., Schmidt, F. A., Krotz, P. D. and Gibson, E. D., *J. Mater. Sci*., 1989, **24**, 1015.
42. Verhoeven, J. D., Chumbley, L. S., Laabs, F. C. and Spitzig, W. A., *Acta metall*., 1991, **39**, 2825.
43. Raabe, D. and Hangen, U., *Comp. Mater. Sci*., 1996, **5**, 195.
44. Trybus, C. and Spitzig, W. A., *Acta metall*., 1989, **37**, 1971.